Proceedings on 23rd Conference on Climate Variability and Change, American Meteorological Society, 23-27 January 2011, Seattle, WA, USA

Upper Ocean Heat Content and Climate Variability

Peter C. Chu

Department of Oceanography, Naval Postgraduate School, Monterey, CA 93943, USA, Email:pcchu@nps.edu

ABSTRACT

Two types of global ocean tripole were identified in the upper layer (0 – 300 m) ocean heat content (OHC) anomaly using the data from the Global Temperature and Salinity Profile Program (GTSPP). First, an optimal spectral decomposition (OSD) scheme was used to build up monthly synoptic temperature and salinity data set for January 1990 to December 2009 on $1^o \times 1^o$ grids and the same 33 vertical levels as the World Ocean Atlas. Then, the monthly varying upper layer OHC field (H_{300}) was obtained. Second, a composite analysis was conducted to obtain the total-time mean OHC field ($\overline{\overline{H}}_{300}$) and the monthly mean OHC variability ($\tilde{H}_{300}$). High $\overline{\overline{H}}_{300}$ (3.0×10^{10} J/m^2) areas are associated with the subtropical gyres. The monthly mean variability $\tilde{H}_{300}$ is an order of magnitude smaller than $\overline{\overline{H}}_{300}$ with a maximum around 2.6×10^9 J/m^2. Third, an empirical orthogonal function (EOF) method is conducted on the residue data ($\hat{H}_{300}$), deviating from $\overline{\overline{H}}_{300} + \tilde{H}_{300}$, in order to obtain interannual variations of the OHC fields. EOF-1 accounts for 44.18% of the variance; and EOF-2 accounts for 14.57% of the variance. They represent two different types of global ocean triple structures with type-1 relating to El Nino events and type-2 relating to pseudo-El Nino and Indian Ocean Dipole events. Significant lag correlation coefficients between the first two principal components and the Southern Oscillation Index were found with maximum values at one month advance of the principal components, which shows the great opportunity of using upper layer OHC for predicting climate variability. At last, the characteristics of the global ocean tripole are insensitive to the selection of upper layer thickness.

***Key Words*— Upper ocean heat content, Global ocean tripole, Optimal spectral decomposition, GTSPP, El Nino, El Nino Modoki, Indian Ocean dipole**

INTRODUCTION

In the past decade, several new coupled ocean-atmosphere phenomena, such as the pseudo-El Nino (or called El Nino Modoki) and the Indian Ocean Dipole (IOD), were discovered and recognized important in climate variability. The pseudo-El Nino is characterized by warmer sea surface temperature anomalies (SSTA) in the central equatorial Pacific and cooler SSTA in the eastern and western equatorial Pacific (Ashok et al. 2007; Weng et al. 2007), which is different from the El Nino with anomalous warming in eastern equatorial Pacific. El Nino and pseudo-El Nino have different teleconnection patterns. Taking the Atlantic Ocean as an example, less tropical storms and hurricanes occur during El Niño events (see the website: http://ww2010.atmos.uiuc.edu/(Gh)/guides/mtr/hurr/enso.rxml); and more tropical storms and hurricanes appear during pseudo-El Nino events (Weng et al. 2007). Ashok et al. (2007) and Weng et al. (2007) described in detail the difference in teleconnections and climate variability between the pseudo-El Nino event in 2004 and El Nino events.

The IOD was identified by Saji et al. (1999) and Vinayachandran et al. (1999). The positive IOD event is characterized by the strong positive sea surface temperature (SST) anomalies (SSTA, relative to mean SST) in the tropical western Indian Ocean (50^oE-70^oE, 10^oS-10^oN, defined as Region A) and the negative SSTA in the southeastern Indian Ocean (90^oE-110^oE, 10^oS-equator, defined as Region B). During negative IOD events, a cold SSTA occurs in the western equatorial Indian Ocean and a warm SSTA appears in the eastern equatorial Indian Ocean, which causes a westerly wind anomaly, and in turn enhances the eastward equatorial jet. During positive IOD events, a warm SSTA occurs in the western equatorial Indian Ocean and a cold SSTA appears in the eastern equatorial Indian Ocean, which causes an easterly wind anomaly, and in turn weakens the EEJ. Chu (2010) confirmed the relationship between IOD and eastward equatorial jet using observational data.

The upper ocean heat content (OHC) variability was recognized important for climate variability in modeling and observational studies. For example, the modeling studies show the effects of OHC on the El Nino – Southern Oscillation (ENSO) events in the equatorial Pacific from different aspects with emphasizing ocean wave propagation process such as the "delayed oscillator" model (Battisti and Hirst 1989), and without emphasizing the detailed wave propagation process

such as the "recharge oscillator" model (Jin 1997). An observational study (Hasegawa and Hanawa 2003) shows the existence of anticlockwise propagation of OHC anomalies in the tropical Northern Pacific, which is closely related to ENSO events.

However, the pseudo-El Nino and IOD events were identified as ocean-atmospheric coupled system from ocean-atmospheric data analysis with SST rather than OHC as a key variable for the ocean. A question arises: Can the three major tropical systems (ENSO, pseudo-El Nino and IOD) be identified from the upper layer (0-300 m) OHC field (H_{300}) along? The reason for the depth of 300 m is that this depth is near the maximum depth to which surface oceanic mixing extends (Chu and Fan 2010). The Global Temperature and Salinity Profile Program (GTSPP) provided the opportunity for answering this question. GTSPP has been developed since 1990 with international cooperation (see the website: http://www.iode.org/). With more observed (T, S) profile data especially with the Argo floats, it is possible to establish gridded (T, S) dataset with a sufficient resolution in space and, especially, in time. From the gridded dataset, it is able to compute global H_{300} at horizontal grids and to analyze its spatial and temporal variability. This paper presents such an effort and is outlined as follows. Section 2 depicts the GTSPP dataset, Section 3 presents characteristics of spatially (1^o resolution) and temporally (1 month increment) varying global H_{300} including seasonal and interannual variations using the composite analysis and the empirical orthogonal (EOF) analysis with EOF-1 connecting to the El Nino events and EOF-2 connecting to the pseudo-El Nino and IOD events. Section 4 shows evident correlations between the principal components of EOF-1 and EOF-2 to the Southern Oscillation Index. It leads to the global ocean tripole concept and its climate impact. Section5 demonstrates the insensitivity of the global ocean tripole to the selection of upper ocean thickness. Section 6 lists the conclusions.

GTSPP

GTSPP is a cooperative international project. It seeks to develop and maintain a global ocean temperature-salinity resource with data that are both up-to-date and of the highest quality possible. Making global measurements of ocean temperature (T) and salinity (S) quickly and easily accessible to users is the primary goal of the GTSPP. Both real-time data transmitted over the Global Telecommunications System, and delayed-mode data received by the National Oceanographic Data Center (NODC) are acquired and incorporated into a continuously managed database. The GTSPP handles all temperature and salinity profile data. This includes observations collected using water samplers, continuous profiling instruments such as Argo floats, CTDs, thermistor chain data and observations acquired using thermosalinographs. The GTSPP went through quality control procedures that make extensive use of flags to indicate data quality. To make full use of this effort, participants of the GTSPP have agreed that data access based on quality flags will be available (Sun et al. 2010). That is, GTSPP participants will permit the selection of data from their archives based on quality flags as well as other criteria. These flags are always included with any data transfers that take place. Because the flags are always included, and because of the policy regarding changes to data, as described later, a user can expect the participants to disseminate data at any stage of processing. Furthermore, GTSPP participants have agreed to retain copies of the data as originally received and to make these available to the user if requested (Sun et al. 2010). Interested readers are referred to the following website (http://www.iode.org/) of the International Oceanographic Commission of UNESCO.

There are total 6,662,209 GTSPP stations with temporally increasing data (Fig. 1). The yearly number of (T, S) profiles is less than 80,000 from 1990 to 1999. Since 2000, as the Argo floats into practice, the yearly number of (T, S) profiles increases exponentially close to 1.7 million in 2009. The GTSPP stations are over the global ocean (Fig. 2a) especially with the Argo floats (Fig. 2b).

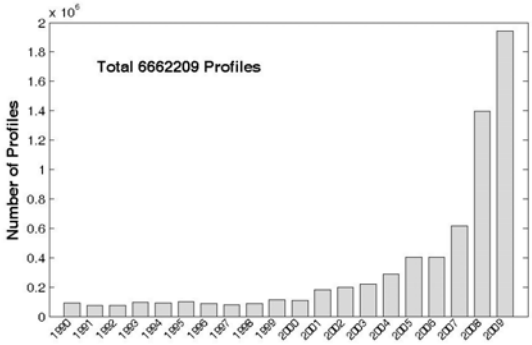

Fig. 1. Temporal distribution of GTSPP stations during 1990-2009 for this study.

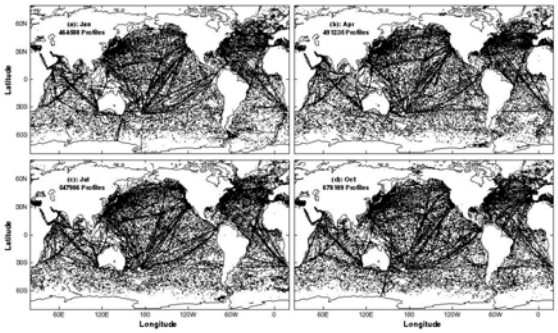

Fig. 2. Spatial distribution of the GTSPP profiles stations during 1990-2009 for (a) January, (b) April, (c) July, and (d) October.

SPATIALLY AND TEMPORALLY VARYING GLOBAL GRIDDED H_{300} DATASET

1.1. Gridded H_{300} Dataset

The OSD method (see Appendix A) is used to establish 3D global gridded (T, S) dataset with monthly increment, $1^o \times 1^o$ horizontal resolution, and 33 vertical layers as the World Ocean Atlas (http://www.nodc.noaa.gov/OC5/WOA05/pr_woa05.html), which is called as the GTSPP gridded data. From the GTSPP gridded dataset, the upper OHC (H_{300}) with the unit of J/m^2 is calculated by

$$H_{300}(\mathbf{r}_i, \tau_k, t_l) = c_p \int_{-300\,m}^{0} \rho T dz\,, \qquad (1)$$

where c_p is the specific heat of the seawater [= 3850 J/(kg K)]; and ρ is the density, which is calculated from the (T, S) data using the equation of the state; the vectors $\mathbf{r}_i$ represent locations of 2D horizontal grids; i = 1, 2, …, I, where I is the total number of the horizontal grid points; τ_k = 1990, 1991, ..., 2009 is the time sequence in years; and t_l = 1, 2, ..., 12 is the monthly sequence within a year.

1.2. Composite Analysis

Before investigating the annual variation of OHC, we define the following two temporal averages:

$$\overline{H}_{300}(\mathbf{r}_i, t_l) = \frac{1}{\Delta\tau}\sum_k H_{300}(\mathbf{r}_i, \tau_k, t_l), \qquad (2a)$$

$\Delta\tau = 20$ (1990 to 2009)

which are the annual mean values, and

$$\overline{\overline{H}}_{300}(\mathbf{r}_i) = \frac{1}{12}\sum_{l=1}^{12} \overline{H}_{300}(\mathbf{r}_i, t_l)\,, \qquad (2b)$$

which are the total-time mean values. The total-time mean (1990-2009) of global upper ocean heat content $\overline{\overline{H}}_{300}(\mathbf{r}_i)$ (Fig. 3) shows following features: (1) it is usually less than 1.2 ×10^{10} J/m^2 north of 40^{o}N and south of 40^{o}S. (2) The high $\overline{\overline{H}}_{300}(\mathbf{r}_i)$ areas are associated with the subtropical gyres in the Atlantic, Pacific, and Indian Oceans. For example, in the Atlantic Ocean, a strong warm core (3.0×10^{10} J/m^2) is located in the Gulf Stream region. It extends northeastward and reaches the northwest African Coast. Another warm area (2.8×10^{10} J/m^2) is located in the South Atlantic with a triangular shape from the Brazilian-Argentine Coast (15^{o}S to 40^{o}S) to the southwest African Coast (around 40^{o}S). Between the two warm regions, there is a cool area (1.9×10^{10} J/m^2) including the equatorial region. In the Pacific Ocean, a warm core in the western North Pacific (the Kuroshio and its extension regions) and the other in the western equatorial/South Pacific with the values around 3.0×10^{10} J/m^2. The eastern Pacific has less values around 2.0×10^{10} J/m^2.

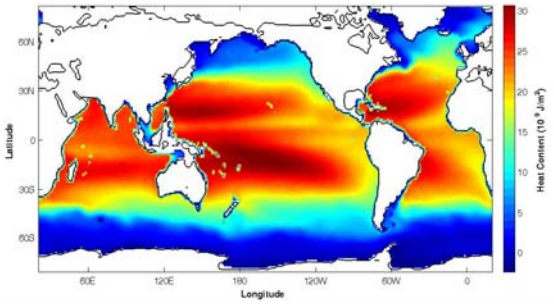

Fig. 3. Total-time mean of global upper ocean heat content $\overline{\overline{H}}_{300}(\mathbf{r}_i)$ during 1990-2009.

The annual mean values deviated from the total-time mean, $\overline{\overline{H}}_{300}(\mathbf{r}_i)$,

$$\tilde{H}_{300}(\mathbf{r}_i, t_l) = \overline{H}_{300}(\mathbf{r}_i, t_l) - \overline{\overline{H}}_{300}(\mathbf{r}_i)\,, \qquad (3)$$

lead to composite features of the mean seasonal variability (Fig. 4). The mean seasonal variability has the following features: (1) $\tilde{H}_{300}(\mathbf{r}_i, t_l)$, with maximum values around 2.6×10^9 J/m^2, is generally an order of magnitude smaller than the total-time mean $\overline{\overline{H}}_{300}(\mathbf{r}_i)$. (2) Its positive values show eddy-like structure and negative values are more spatially uniform. (3) Usually, negative (positive) values occur in the northern (southern) hemisphere in boreal winter (Fig. 4a) and spring (Fig. 4b), and positive (negative) values occur in the northern (southern) hemisphere in boreal summer (Fig. 4c) and fall (Fig. 4d).

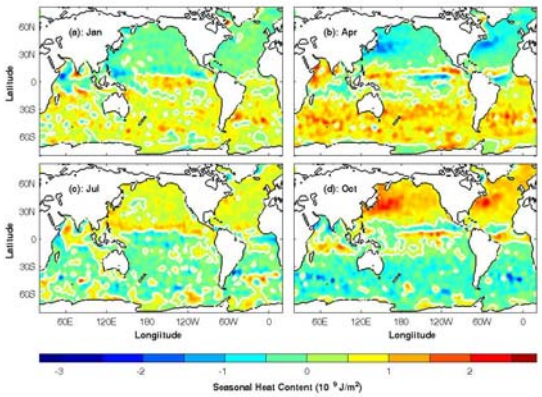

Fig. 4. Mean seasonal variability of upper layer heat content $\tilde{H}_{300}(\mathbf{r}_i, t_l)$ (unit: J/m^2) : (a) January, (b) April, (c) July, and (d) October.

1.3. OHC Anomaly

OHC anomaly is the deviation of H_{300} from its annual mean value

$$\hat{H}_{300}(\mathbf{r}_i, \tau_k, t_l) = H_{300}(\mathbf{r}_i, \tau_k, t_l) - \overline{H}_{300}(\mathbf{r}_i, t_l), \qquad (4)$$

which is re-arranged into a N×P matrix, $\hat{H}_{300}(\mathbf{r}_i, \tilde{t}_p)$, p = 1, 2, …, *P*. Here *P* = 240 is the total number of months (i.e., total time points). The empirical orthogonal function (EOF) analysis (Lorenz 1956) was conducted on the heat content anomaly data

$$\hat{H}_{300}(\mathbf{r}_i, \tilde{t}_p) = \sum_j PC_j(\tilde{t}_p) E_j(\mathbf{r}_i), \qquad (5)$$

where $E_j(\mathbf{r}_i)$ is the jth EOF mode with the unit of J/m^2; and $PC_j(\tilde{t}_p)$ is the jth principal component without unit. Here, j = 1, 2, …, *J*; *J* is truncated number of the EOF modes. Table-1 shows the variance for the first six EOFs with EOF-1containing 44.18% of variance and EOF-2 containing 14.57% of variance. Here, the effort is concentrated on analyzing the first 2 EOF modes.

Table 1. Variances of the first six leading EOFs of $\hat{H}_{300}$.

EOF	Variance	Cumulative Variance
1	0.4418	0.4418
2	0.1457	*0.5875*
3	0.0620	0.6495
4	0.0447	0.6942
5	0.0304	0.7246
6	0.0274	0.7520

1.4. EOF-1 Mode

The EOF-1 mode (Fig. 5) shows a global ocean triple structure (i.e., positive-negative-positive): The western Pacific (near half of the Pacific Ocean) and the Indian Ocean are positive with a strong maximum center located at the western tropical Pacific warm pool region north of New Guinea with maximum value higher than 2.0×10^9 J/m^2. Vast area of the Indian Ocean is positive with maximum value less than 0.7×10^9 J/m^2. The eastern Pacific is negative with minimum value lower than -0.5×10^9 J/m^2 located in the east equatorial Pacific. The whole Atlantic is positive with low values ($0.1 - 0.4\times10^9$ J/m^2). This pattern is the positive phase of the type-1 tripole.

The first principal component for 1990-2009, $PC_1(\tilde{t}_p)$, fluctuates between -1 to 1, which makes the magnitude of the EOF-1 pattern around 2.0×10^9 J/m^2, comparable to the magnitude of the seasonal variability (2.6×10^9 J/m^2). It has an evident upward trend with $PC_1(\tilde{t}_p) < 0$ before 1998 and $PC_1(\tilde{t}_p) > 0$ after 1999 except 2002 (Fig. 6). For $PC_1(\tilde{t}_p) > 0$, the horizontal variability of OHC anomaly shows the positive phase of the type-1 tripole pattern given in Fig. 5 (i.e., positive-negative-positive). For the equatorial Pacific, this [i.e., $PC_1(\tilde{t}_p) > 0$] represents La Nina. For the Indian and Atlantic Oceans, this shows warm anomalies. For $PC_1(\tilde{t}_p) < 0$, the horizontal variability of OHC anomaly shows the negative phase of the type-1 tripole pattern (i.e., opposite as shown in Fig. 5). That is, negative anomalies occupy the whole Indian Ocean and the western Pacific; positive anomalies occur in the eastern Pacific; and negative anomalies occupy the whole Atlantic Ocean. For the equatorial Pacific, this [i.e., $PC_1(\tilde{t}_p) < 0$] represents the El Nino events. The values of $PC_1(\tilde{t}_p)$ are generally negative in 1990-1998. During this period, $PC_1(\tilde{t}_p)$ has minimum value in 1991-1992, 1993, 1995, and 1997-1998. They correspond to 1991-1995 long El Nino event, and 1997-1998 El Nino event. The values of $PC_1(\tilde{t}_p)$ are positive in 1999-2009, which implies that there is no El Nino event (in the classical sense) during this period. Taking 1997-1998 El Nino event as an example, $PC_1(\tilde{t}_p)$ is -1.0 in November 1997. The OHC has warm anomaly greater than 0.50×10^9 J/m^2 in the eastern Pacific; cold anomaly in the western Pacific and vast area of the Indian Ocean with the minimum around -0.60×10^9 J/m^2; and weak cold anomaly in the whole Atlantic with anomalies around -0.40×10^9 J/m^2 in the tropics. Such features show less (more) heat stored in the upper layers of the western Pacific Ocean, Indian Ocean, and Atlantic Ocean during El Nino (La Nina) events. This may lead to less (more) tropical cyclone damage during El Nino (La Nina) events in the tropical Atlantic, which is consistent with earlier results (Pielke and Landsea 1999).

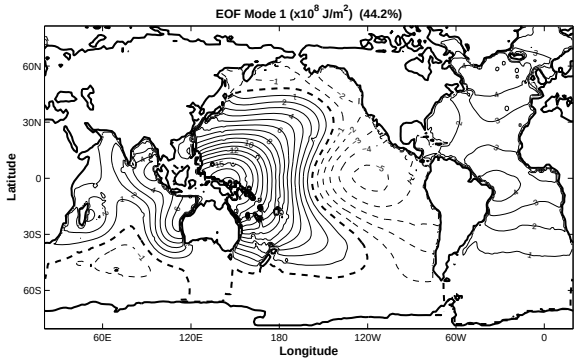

Fig. 5. EOF-1 of the OHC anomaly $\hat{H}_{300}$ (unit: 10^8 J/m^2).

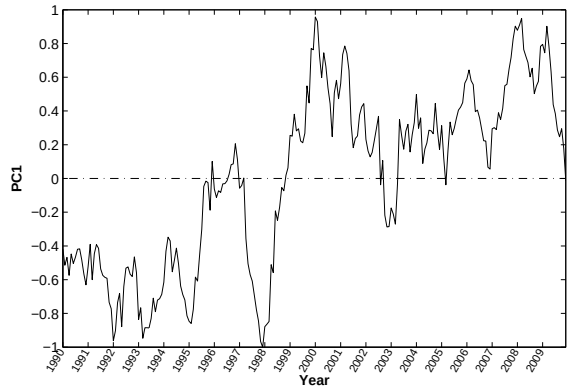

Fig. 6. Time series of principal component for the EOF-1 mode of the OHC anomaly $\hat{H}_{300}$.

1.5. EOF-2 Mode

The EOF-2 mode (Fig. 7) shows a different global ocean triple structure (i.e., negative-positive-negative): The western Pacific (small portion of the Pacific Ocean) and the southeastern Indian Ocean are positive with a maximum (around 0.45×10^9 J/m^2) located near the Indonesian islands and a maximum (around 0.30×10^9 J/m^2) located near the southwest coast of Australia. This positive area is sandwiched by two negative areas with one in the western Indian Ocean, and the other in the central/eastern Pacific Ocean, and the Atlantic Ocean. A minimum value around -0.8×10^9 J/m^2 appears in the equatorial central Pacific (130°W - 120°W, 3°N - 3°S). This is called the type-2 tripole.

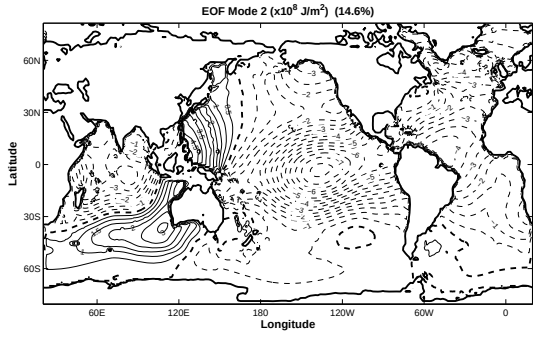

Fig. 7. EOF-2 of the OHC anomaly $\hat{H}_{300}$ (unit: 10^8 J/m^2).

The second principal component, $PC_2(\tilde{t}_p)$, fluctuates between -1 to 1 during 1990-2009, which makes the magnitude of the EOF-2 pattern around 0.8×10^9 J/m^2, a little smaller than the magnitude of the seasonal variability (2.6×10^9 J/m^2). Different from $PC_1(\tilde{t}_p)$, the second principal component, $PC_2(\tilde{t}_p)$, does not have a trend (Fig. 8). For $PC_2(\tilde{t}_p) > 0$, the horizontal variability of OHC anomaly shows the positive phase of the type-2 tripole given in Fig. 6 (i.e., negative-positive-negative). For the equatorial Pacific, this [i.e., $PC_2(\tilde{t}_p) > 0$] represents La Nina. For the Indian Ocean, this represents negative IOD mode. For $PC_2(\tilde{t}_p) < 0$, the horizontal variability of OHC anomaly shows the negative phase of the type-2 tripole pattern (i.e., opposite as shown in Fig. 7). That is, negative OHC anomalies occupy the western Pacific (small portion of the Pacific Ocean) and the southeastern Indian Ocean; positive OHC anomalies occupy rest of the oceans. This [i.e., $PC_2(\tilde{t}_p) < 0$] represents the pseudo-El Nino events in the equatorial Pacific with the maximum OHC occurring in the central equatorial Pacific, positive IOD mode in the Indian Ocean, and positive OHC anomalies in the whole Atlantic Ocean, which may increase the activities of tropical cyclones in the Atlantic (Weng et al., 2007).

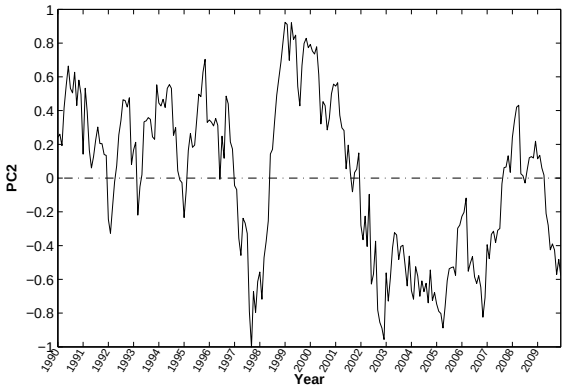

Fig. 8. Time series of principal component for the EOF-2 mode of the OHC anomaly $\hat{H}_{300}$.

$PC_2(\tilde{t}_p)$ was negative in short periods in 1992, 1993, and 1996, January 1997 to July 1998, March 2002 to February 2007, and the whole year of 2009. Among them, the period of January 1997 to July 1998 is very special, when both $PC_1(\tilde{t}_p)$ and $PC_2(\tilde{t}_p)$ are negative, which implies an El Nino event from the EOF-1 and a pseudo-El Nino event from the EOF-2. Furthermore, the value of $PC_2(\tilde{t}_p)$ is -1.0 in October 1997. The OHC of the EOF-2 mode has warm anomaly greater than 0.8×10^9 J/m^2 in the central Pacific; cold anomalies in the western Pacific with a minimum around -0.45×10^9 J/m^2 near Indonesian islands and in the southeastern Indian Ocean with a minimum around -0.3×10^9 J/m^2 near southwest of Australia; and warm anomalies in the western Indian Ocean with a maximum around 0.3×10^9 J/m^2 near Somali Coast; and in the whole Atlantic Ocean with a maximum around 0.4×10^9 J/m^2 in the western tropical Atlantic near northeast African Coast.

CONNECTION TO CLIMATE VARIABILITY

Climate systems are complex. One way to simplify the climate systems is to represent climate variability of atmospheric circulations by teleconnection patterns, such as the Southern Oscillation Index (SOI), the Arctic Oscillation (AO), Antarctic Oscillation (AAO), North Atlantic Oscillation (NAO), and Pacific–North American pattern (PNA). Here, we take the SOI as an example to show the connection of the OHC anomalies to the climate variability.

1.6. Southern Oscillation Index

The SOI, represented by $s(\tilde{t}_p)$, was first to utilize equivalent barotropic seesaw in atmospheric pressure between the southeastern tropical Pacific and the Australian–Indonesian regions (Walker and Bliss 1937). A popular formula for calculating the monthly SOI is proposed by the Australian Bureau of Meteorology:

$$s(\tilde{t}_p) = 10 \times \frac{p_{diff}(\tilde{t}_p) - \left\langle p_{diff} \right\rangle}{SD(p_{diff})}. \qquad (6)$$

Here, p_{diff} is the mean sea level pressure of Tahiti minus that of Dawin for that month; $\left\langle p_{diff} \right\rangle$ is the long-term average of p_{diff} for the month in question; and SD(p_{diff}) is the long-term standard deviation of p_{diff} for the month in question. The SOI (Fig. 9) ranges from about -35 to about 35. Positive values of the SOI are associated with stronger Pacific trade winds and warmer sea temperatures to the north of Australia. Together these give a high probability that eastern and northern Australia will be wetter than normal. During El Niño episodes, the Walker circulation weakens, seas around Australia cool, and slackened trade winds feed less moisture into the Australian/Asian region. There is then a high probability that eastern and northern Australia will be drier than normal.

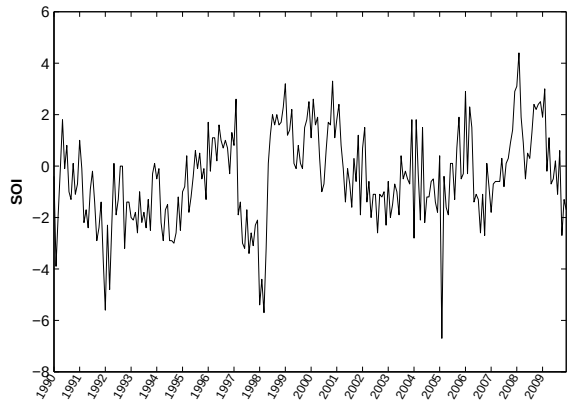

Fig. 9. Time series of SOI.

1.7. Lag-Correlations between SOI and Principal Components

Linkage between the OHC anomaly and climate variability is represented by the lag-correlation coefficients between the climate indices (such as SOI) with the principal components $PC_1(\tilde{t}_p)$ and $PC_2(\tilde{t}_p)$. The total size of the time series (n) is 240 (20 years of monthly data between 1990 and 2009). The significance of the correlation coefficient r can be tested by the quantity

$$t = r\sqrt{\frac{n-2}{1-r^2}}, \qquad (10)$$

which approximately satisfies the t-distribution with degree of freedom of (n - 2). The critical value for the lag-correlation coefficient is 0.197 for n = 240, and $\alpha = 0.01$.

The lag-correlation coefficients between $s(\tilde{t}_p)$ and $PC_1(\tilde{t}_p)$ show evident association with a maximum value of 0.63 at one month lead of $PC_1(\tilde{t}_p)$. The correlation decreases as the lag interval increases, but still larger than the critical value of 0.197 from 14-month lead to 10- month lag of $PC_1(\tilde{t}_p)$ to $s(\tilde{t}_p)$ (Fig. 10a). The lag-correlation coefficients between $s(\tilde{t}_p)$ and $PC_2(\tilde{t}_p)$ show evident association with a maximum value of 0.42 at one month lead of $PC_2(\tilde{t}_p)$. It decreases as the lag interval increases, but still larger than the critical value of 0.197 with 5- month lead to 5-month lag of $PC_2(\tilde{t}_p)$ to $s(\tilde{t}_p)$ (Fig. 10b). This suggests that both EOF-1 and EOF-2 modes are related to the Southern Oscillation with a maximum correlation at month lead. This also implies the capability of OHC on the prediction of El Nino, pseudo-El Nino, and IOD events.

Fig. 11 shows such a link between the first mode of the OHC anomaly and the zonal atmospheric circulations. During the positive phase of $PC_1(\tilde{t}_p)$, the type-1 tripole is in the positive phase. Positive OHC anomalies occupy the whole Indian Ocean, the whole Atlantic Ocean, and the western Pacific with a maximum OHC occurring north of New Guinea; and negative OHC anomalies occupy the eastern Pacific. Such a zonal asymmetric OHC pattern in the tropics may lead to anomalous two-cell Walker circulations in the whole tropical atmosphere with a strong downward branch in the eastern Pacific, weak upward branches in the Atlantic and Indian oceans, and strong upward branch in the western Pacific (Fig. 11a). For the Pacific Ocean, it is a typical La Nina event. During the negative

phase of $PC_1(\tilde{t}_p)$, the type-1 tripole is in the negative phase. Negative OHC anomalies occupy the whole Indian Ocean, the whole Atlantic Ocean, and the western Pacific with a minimum OHC occurring north of New Guinea; and positive OHC anomalies occupy the eastern Pacific. Such a zonal asymmetric OHC pattern in the tropics may lead to opposite anomalous two-cell Walker circulations in the whole tropical atmosphere with a strong downward branch in the western Pacific, weak downward branches in the Atlantic and Indian oceans, and strong upward branch in the eastern Pacific (Fig. 11b). For the Pacific Ocean, it is a typical El Nino event. The anomalous vertical circulations shown in Fig. 11 may be called the type-1 two-cell Walker circulations.

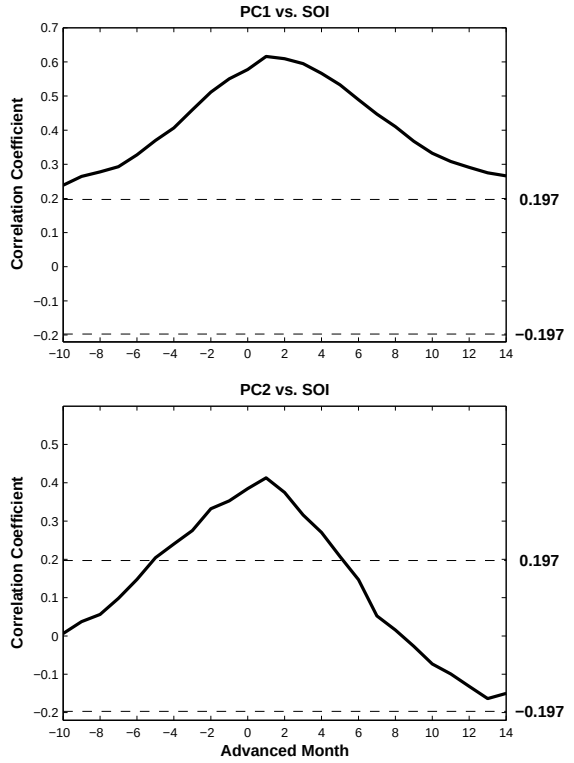

Fig. 10. Lag correlation coefficients between SOI and (a) PC_1, (b) PC_2 with positive time denoting lag of SOI.

Fig. 12 shows such a link between the second mode of the OHC anomaly and the zonal atmospheric circulations. During the positive phase of $PC_2(\tilde{t}_p)$, the type-2 tripole is in the positive phase. Positive OHC anomalies occupy the western Pacific (small portion of the Pacific Ocean) and the southeastern Indian Ocean with a maximum center located near the Indonesian islands; negative OHC anomalies occupy the western Indian Ocean, the whole Atlantic Ocean, and the central-eastern Pacific Ocean with a minimum OHC anomaly occurring in the central Pacific Ocean. Such a zonal asymmetric OHC pattern in the tropics may lead to anomalous two-cell Walker circulations in the whole tropical atmosphere with a strong upward branch in the western Pacific Ocean and the southeastern Indian Ocean, strong downward branch in the central Pacific Ocean, weak downward branches in the western Indian Ocean, eastern Pacific Ocean, and Atlantic Ocean. This refers to the La Nina in the equatorial Pacific Ocean, and negative IOD event in the Indian Ocean (Fig. 12a).

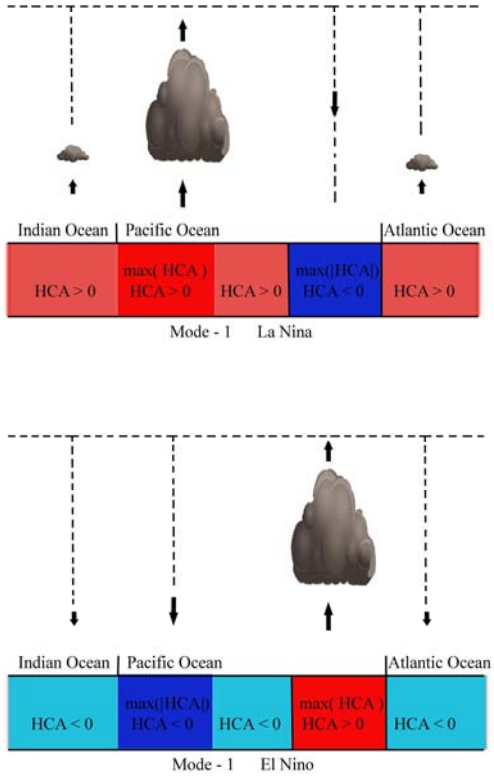

Fig. 11. The first mode of global ocean tripole: (a) positive and (b) negative phases.

During the negative phase of $PC_2(\tilde{t}_p)$, the type-2 tripole is in the negative phase. Negative OHC anomalies occupy the western Pacific and the southeastern Indian Ocean with a minimum center located near the Indonesian islands; positive OHC anomalies occupy the western Indian Ocean, the whole Atlantic Ocean, and the central-eastern Pacific Ocean with a minimum OHC anomaly occurring in the central Pacific Ocean. Such a zonal asymmetric OHC pattern in the tropics may lead to anomalous two-cell Walker circulations in the whole tropical atmosphere with a strong downward branch in the western Pacific Ocean and the southeastern Indian Ocean, strong upward branch in the central Pacific Ocean, weak upward

ranches in the western Indian Ocean, eastern Pacific Ocean, and Atlantic Ocean. This refers to pseudo-El Nino in the equatorial Pacific Ocean, and positive IOD event in the Indian Ocean (Fig. 12b). The anomalous vertical circulations shown in Fig. 12 may be called the type-2 two-cell Walker circulations. Such a two-cell Walker circulations were identified by Yamamoto et al. (2007) for the Pacific Ocean.

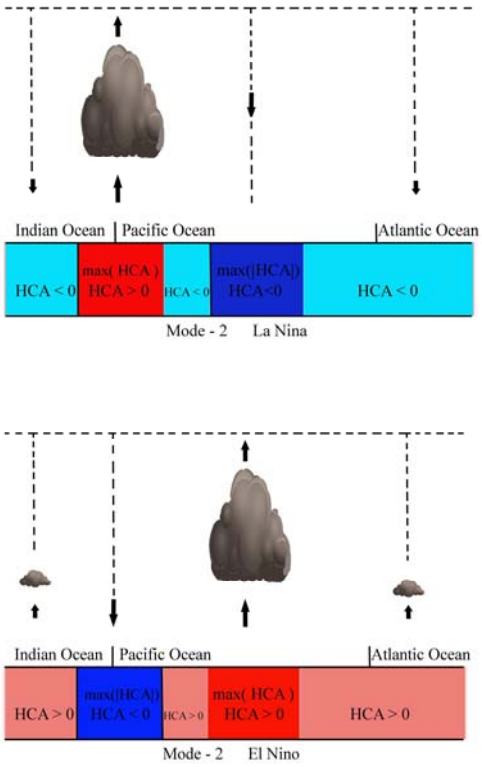

Fig. 12. The second mode of global ocean tripole: (a) positive and (b) negative phases.

1.8. Phase Space Trajectory

Temporal variation of the two modes can be obtained by plotting the pair data $[PC_1(\tilde{t}_p), PC_2(\tilde{t}_p)]$ in the phase diagram with PC_1 as the horizontal axis and PC_2 as the vertical axis (Fig. 13). The trajectory in the phase space starts from January 1990 [90 enclosed by a circle)] to December 2009 (a star enclosed by a circle). In Fig. 13, the number enclosed by a circle denotes January of the year (90 means 1990, …); the arrows show the time advancement; the red color refers to negative values of SOI and blue color refers to positive values of SOI. The trajectory represents evolution of the OHC anomaly in various phases relating to climate variability. For the trajectories between two consecutive years in the quadrant of (+, +) such as 99-00-01 (representing January 1999 to January 2002), 08-09 (representing January 2008 to January 2009), both EOF-1 and EOF-2 modes are in the positive phase, which implies La Nino in the tropical Pacific and negative IOD in the Indian Ocean. For the trajectories between two consecutive years in the quadrant of (-, -) such as 97-98, both EOF-1 and EOF-2 modes are in the negative phase, which implies El Nino and pseudo-El Nino in the tropical Pacific and positive IOD in the Indian Ocean. For the trajectories between two consecutive years in the quadrant of (+, -) such as 04-05-06-07, and most months in 2009, the EOF-1 mode is in the positive phase and the EOF-2 mode is in the negative phase, which implies pseudo-El Nino in the tropical Pacific and positive IOD in the Indian Ocean. For the trajectories between two consecutive years in the quadrant of (-, +) such as most months in 1990-1995, the EOF-1 mode is in the negative phase and the EOF-2 mode is in the positive phase or near zero such as 92 and 95, which implies El Nino in the tropical Pacific and negative IOD in the Indian Ocean.

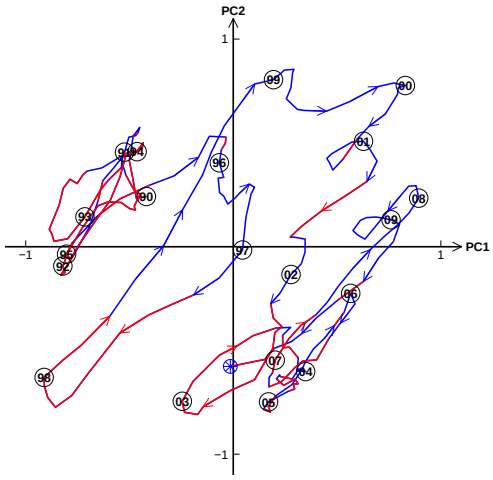

Fig. 13. Trajectory in the phase space (PC_1, PC_2) from January 1990 to December 2009 (a star enclosed by a circle). Here, the number enclosed by a circle denotes January of the year (90 means 1990, …); the arrows show the time advancement; the red color refers to negative values of SOI and blue color refers to positive values of SOI.

INSENSITIVITY OF THICKNESS SELECTION

This study chooses 300 m as the upper layer thickness. To show the insensitivity of such a selection on the global ocean tripole structure, the upper layer (0-700 m) OHC (H_{700}) is calculated from the GTSPP gridded data,

$$H_{700}(\mathbf{r}_i, \tau_k, t_l) = c_p \int_{-700m}^{0} \rho T dz \,. \qquad (11)$$

Same as in Section 3, the total-time mean OHC $\overline{\overline{\mathrm{H}}}_{700}(\mathbf{r}_i)$ (Fig. 14) and the mean seasonal variability $\tilde{\mathrm{H}}_{700}(\mathbf{r}_i, t_l)$ (Fig. 15) were calculated. Comparisons between Fig. 14 and Fig. 3, Fig. 15 and Fig. 4 show very similar structures. For example, Fig. 14 shows that (1) $\overline{\overline{\mathrm{H}}}_{700}(\mathbf{r}_i)$ is usually less than 2.0 $\times 10^{10}$ J/m^2 north of 40^{o}N and south of 40^{o}S. (2) The high $\overline{\overline{\mathrm{H}}}_{700}(\mathbf{r}_i)$ areas are associated with the subtropical gyres in the Atlantic, Pacific, and Indian Oceans. A strong warm core (5.4×10^{10} J/m^2) is located in the Gulf Stream region, which extends northeastward and reaches the northwest African Coast. Another warm area (4.2×10^{10} J/m^2) is located in the South Atlantic with a triangular shape from the Brazilian-Argentine Coast (15^{o}S to 40^{o}S) to the southwest African Coast (around 40^{o}S). Between the two warm regions, there is a cool area (3.2×10^{10} J/m^2) including the equatorial region. Fig. 15 demonstrates similar features of the mean seasonal variability $\tilde{\mathrm{H}}_{700}(\mathbf{r}_i, t_l)$ as compared to $\tilde{\mathrm{H}}_{300}(\mathbf{r}_i, t_l)$: (1) $\tilde{\mathrm{H}}_{700}(\mathbf{r}_i, t_l)$, with maximum values around 5.6×10^9 J/m^2, is generally an order of magnitude smaller than the total-time mean $\overline{\overline{\mathrm{H}}}_{700}(\mathbf{r}_i)$. (2) Its positive values show eddy-like structure and negative values are more spatially uniform. (3) Usually, negative (positive) values occur in the northern (southern) hemisphere in boreal winter (Fig. 15a) and spring (Fig. 15b), and positive (negative) values occur in the northern (southern) hemisphere in boreal summer (Fig. 15c) and fall (Fig. 15d). (4) A near zonal belt of positive values (around 2.0×10^9 J/m^2) is located in the equatorial oceans. The tripole structures were also identified from the OHC anomaly $\hat{\mathrm{H}}_{700}(\mathbf{r}_i, \tilde{t}_p)$ using the EOF analysis. Table-2 shows the variance for the first six EOFs with EOF-1containing 49.75% of variance and EOF-2 containing 11.82% of variance. Here, the effort is concentrated on analyzing the first 2 EOF modes.

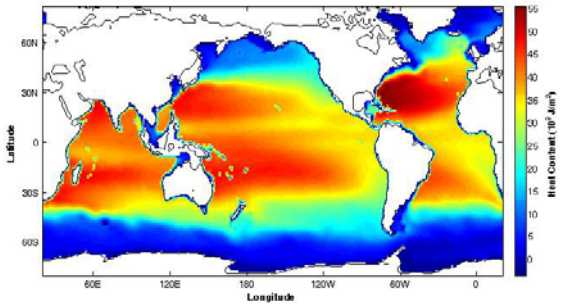

Fig. 14. Total-time mean of global upper ocean heat content $\overline{\overline{\mathrm{H}}}_{700}(\mathbf{r}_i)$ during 1990-2009.

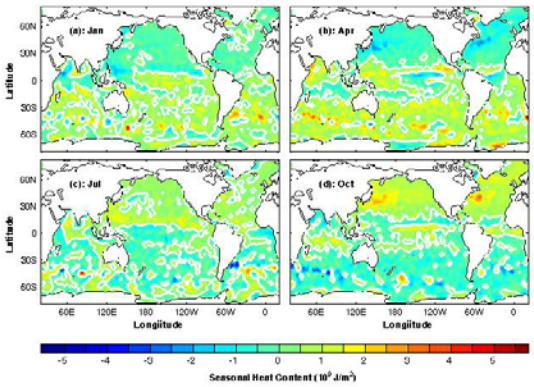

Fig. 15. Mean seasonal variability of upper layer heat content $\tilde{\mathrm{H}}_{700}(\mathbf{r}_i, t_l)$ (unit: J/m^2) : (a) January, (b) April, (c) July, and (d) October.

Table 2. Variances of the first six leading EOFs of $\hat{\mathrm{H}}_{700}$

EOF	Variance	Cumulative Variance
1	0.4975	0.4975
2	0.1182	0.6157
3	0.0499	0.6656
4	0.0377	0.7033
5	0.0259	0.7292
6	0.0233	0.7525

The EOF-1 mode (Fig.16) shows a similar type-1 tripole as depicted in Fig. 5 (i.e., positive-negative-positive): The western Pacific (near half of the Pacific Ocean) and the Indian Ocean are positive with a strong maximum center located at the western tropical Pacific warm pool region north of New Guinea with maximum value higher than 2.2×10^9 J/m^2. Vast area of the Indian Ocean is positive with maximum value less than 0.7 $\times10^9$ J/m^2. The eastern Pacific is negative with minimum value lower than -0.4 $\times10^9$ J/m^2 located in the east equatorial Pacific. The whole Atlantic is positive with low values (0.2 - 0.8$\times10^9$ J/m^2). The first principal component for 1990-2009, $PC_1(\tilde{t}_p)$, fluctuates between -1 to 1. It has evident upward trend with $PC_1(\tilde{t}_p) < 0$ before 1999 and $PC_1(\tilde{t}_p) > 0$ after 1999 (Fig. 17). The temporal variations of $PC_1(\tilde{t}_p)$ for $\hat{\mathrm{H}}_{700}(\mathbf{r}_i, \tilde{t}_p)$ and for $\hat{\mathrm{H}}_{300}(\mathbf{r}_i, \tilde{t}_p)$ are very similar.

The EOF-2 mode (Fig.18) shows a similar type-2 tripole as depicted in Fig. 7 (i.e., negative-positive-negative): The western Pacific (small portion of the Pacific Ocean) and the southeastern Indian Ocean are positive with a maximum (around 0.9×10^9 J/m^2) located near the Indonesian islands and a maximum (around 0.6×10^9 J/m^2) located near the southwest coast of Australia. This positive area is sandwiched by two

negative areas with one in the western Indian Ocean, and the other in the central/eastern Pacific Ocean, and the Atlantic Ocean. A minimum value around 1.2×10^9 J/m^2 appears in the equatorial central Pacific (130°W - 118°W, 3°N - 3°S). The second principal component, $PC_2(\tilde{t}_p)$, fluctuates between -1 to 1 during 1990-2009. The temporal variations of $PC_2(\tilde{t}_p)$ for $\hat{H}_{700}(\mathbf{r}_i,\tilde{t}_p)$ and for $\hat{H}_{300}(\mathbf{r}_i,\tilde{t}_p)$ are very similar. For example, $PC_2(\tilde{t}_p)$ was negative in boreal summers (June, July, August, September) of 1991, 1992, and 1994, January 1997 to November 1998, March 2002 to February 2007, and the whole year of 2009.

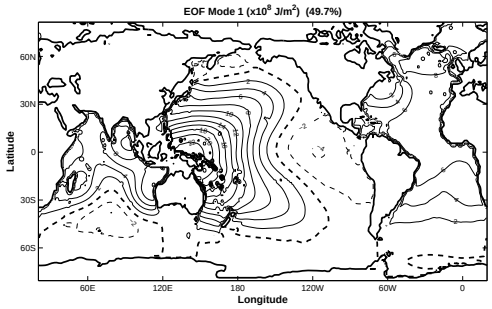

Fig. 16. EOF-1 of the OHC anomaly $\hat{H}_{700}$ (unit: 10^8 J/m^2).

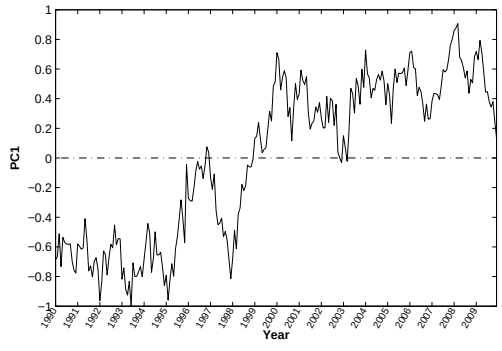

Fig. 17. Time series of principal component for the EOF-1 mode of the OHC anomaly $\hat{H}_{700}$.

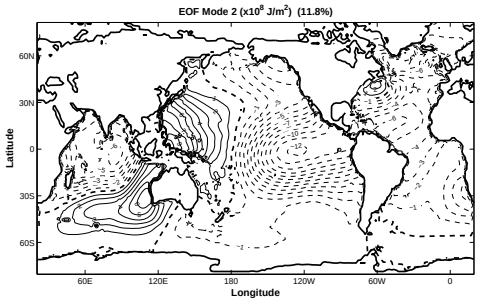

Fig. 18. EOF-2 of the OHC anomaly $\hat{H}_{700}$ (unit: 10^8 J/m^2).

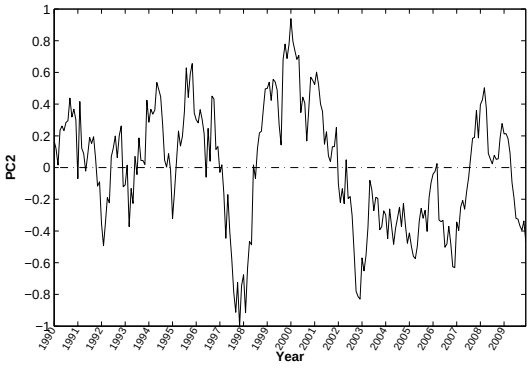

Fig. 19. Time series of principal component for the EOF-2 mode of the OHC anomaly $\hat{H}_{700}$.

CONCLUSIONS

The goal of this study was to identify the interannual variability in the upper ocean (0 – 700 m) heat content (H_{300}) from analysis of the global temperature and salinity profile program (GTSPP) data. The optimal spectral decomposition (OSD) method, composite analysis, and EOF analysis were used. The following results were obtained from this observational study:

(1) The total-time mean OHC field ($\overline{\overline{H}}_{300}$) was established with OHC less than 1.2×10^9 J/m^2 north of 40°N and south of 40°S. The high $\overline{\overline{H}}_{300}(\mathbf{r}_i)$ areas are associated with the subtropical gyres in the Atlantic, Pacific, and Indian Oceans with OHC ranging from 2.8 to 3.0×10^{10} J/m^2. The OHC is less outside than inside of the subtropical gyres in the same latitudinal zone, such as in the eastern Pacific (around 2.0×10^{10} J/m^2).

(2) The composite analysis indicates the following features of the mean seasonal variability of OHC (i.e., annual mean OHC relative to the total-time mean OHC). The maximum seasonal variability is around 2.6×10^9 J/m^2, which is an order of magnitude smaller than the total-time mean $\overline{\overline{H}}_{300}(\mathbf{r}_i)$. Positive variability (summer and fall) shows eddy-like structure and negative variability (winter and spring) is more spatially uniform.

(3) The EOF analysis was applied to the OHC anomaly data (removal of total-time mean and mean seasonal variability) to identify low-frequency variability of the OHC anomaly. EOF-1 accounts for 44.18% of variance and EOF-2 accounts for 14.57% of variance. Both modes show the global ocean triple structure with the type-1 tripole for EOF-1 and the type-2 tripole for the EOF-2. The type-1 tripole has comparable order of magnitudes as the seasonal variability, while the type-2 tripole has smaller magnitudes compared to the seasonal variability.

(4) Positive phase of the type-1 tripole refers to the La Nina in the equatorial Pacific with positive OHC anomalies in the whole Atlantic and Indian Oceans. Negative phase of the type-1 tripole refers to the El Nino in the equatorial Pacific with negative OHC anomalies in the whole Atlantic and Indian Oceans. Positive phase of the type-2 tripole refers to the La Nina in the equatorial Pacific, the negative IOD event in the Indian Ocean, and negative OHC anomaly in the whole Atlantic Ocean. Negative phase of the type-2 tripole refers to the pseudo-El Nino in the equatorial Pacific, the positive IOD event in the Indian Ocean, and positive OHC anomaly in the whole Atlantic Ocean.

(5) The global ocean tripole was identified from the upper OHC. This implies that upper ocean takes a key role in climate variability. Significant lag correlation coefficients between (PC_1, PC_2) and SOI with maximum values at one month advance of (PC_1, PC_2) shows that the potential of using upper layer OHC for predicting global scale low frequency phenomena such as El Nino, pseudo-El Nino, and IOD events. Recently, there are 3193 Argo floats spreading out over the world oceans (Fig. 2b). It is possible to provide gridded OHC data on time, and hopefully to improve the prediction of these phenomena.

(6) The results obtained here are not sensitive to the selection of the upper ocean thickness for computing the OHC. The two types of the global ocean tripole indentified from the first two leading EOFs of the OHC anomaly are very similar between the layer thickness chosen as 300 m and as 700 m.

APPENDIX A. PTIMAL SPECTRAL DECOMPOSITION

A new data analysis/assimilation scheme, the optimal spectral decomposition (OSD), has been recently developed to analyze fields from noisy and sparse oceanographic data. Let ($\mathbf{x}$, z) be horizontal and vertical coordinates and t be time. A physical variable $c(\mathbf{x}, z, t)$ at depth z_k is decomposed using the generalized Fourier series (Chu 1999; Chu et al. 2003a, b, 2005a, b; Ivanov and Chu 2008)

$$c(\mathbf{x}, z_k, t) = c_0(z_k, t) + \sum_{m=1}^{M} a_m(z_k, t)\, \Phi_m(\mathbf{x}, z_k), \quad \mathbf{x} \in R(z_k) \tag{A1}$$

where c_0 is the horizontal mean of the variable c. M is the truncated mode number, $\Phi_m(\mathbf{x}, z_k)$ and $a_m(z_k, t)$ are the orthogonal basis functions (or called modes) and the spectral coefficients, respectively; $R(z_k)$ is the area bounded by the lateral boundary $\Gamma(z_k)$ at depth z_k. The basis functions $\{\Phi_m(\mathbf{x}, z_k)\}$ are eigen-functions of the horizontal Laplace operator ($\nabla_h^2 \equiv \partial^2/\partial x^2 + \partial^2/\partial y^2$) with the basin geometry and certain physical boundary conditions. For temperature and salinity, the homogeneous Neumann boundary condition is taken at the solid boundary $\Gamma(z)$ (i.e., no heat and salt fluxes),

$$\nabla_h^2 \Phi_m = -\lambda_m \Phi_m, \quad \mathbf{n} \bullet \nabla_h \Phi_m \,|_\Gamma = 0, \quad m = 1, 2, ..., M, \tag{A2}$$

where $\mathbf{n}$ is the unit vector normal to $\Gamma(z)$. The basis functions $\{\Phi_m\}$ are independent of the data and therefore available prior to the data analysis. The OSD method has two important procedures: optimal mode truncation and determination of spectral coefficients $\{a_m\}$. The optimal mode truncation (M) is determined using Vapnik (1982) variational method. Application of the generalized Fourier series expansion (1) to the observational points with P as the total number of observations leads to an algebraic equation

$$\mathbf{Aa} = \mathbf{QY}. \tag{A3}$$

where $\mathbf{a} = (a_1, a_2, \ldots, a_M)$, is the state vector ($M$-dimensional) ; $\mathbf{A}$ is a $P \times M$ matrix; $\mathbf{Q}$ is a $P \times P$ square matrix ($P > M$); $\mathbf{Y}$ is a P-dimensional observation vector, consisting of a signal $\overline{\mathbf{Y}}$ and a noise $\mathbf{Y'}$. Due to high level of noise contained in the observations, the algebraic equation (3) is ill-posed and needs to be solved by a rotation matrix regularization method (Chu et al. 2004) that provides: (a) stability (robustness) even for data with high noise, and (b) the ability to filter out errors with a-priori unknown statistics. Interested readers are referred to Chu et al. (2003 a, b; 2004).

ACKNOWLEDGMENTS

The Office of Naval Research, the Naval Oceanographic Office, and the Naval Postgraduate School supported this study. The author thanks Dr. Noden E. Huang at the National Central University in Taiwan for stimulating discussion, Dr. L. Charles Sun at NOAA/NODC for providing the GTSPP data, and Mr. Chenwu Fan at NPS for computing assistance.

REFERENCES

Ashok K, Behera S, Rao A. S, Weng H., and Yamagata, T., 2007. El Nino Modoki and its teleconnection. J. Geophys. Res., 112, C11007, doi:10.1029/2006JC003798.

Battisti, D. S., and Hirst, A. C., 1989. Interannual variability in a tropical atmosphere–ocean model: Influence of the basic state, ocean geometry and nonlinearity. *J. Atmos. Sci.,* **46,** 1687–1712.

Chu, P.C., 2010. Observational studies on association between eastward equatorial jet and Indian Ocean dipole. *J. Oceanogr.,* 66, 429-434.

Chu, P. C., Ivanov, L. M., Korzhova, T. P., Margolina, T. M., and Melnichenko, O. M., 2003a. Analysis of sparse and noisy ocean current data using flow decomposition. Part 1: Theory. *J. Atmos. Oceanic Technol.*, 20, 478-491.

Chu, P. C., Ivanov, L. M., Korzhova, T. P., Margolina, T. M., and Melnichenko, O. M., , 2003b. Analysis of sparse and noisy ocean current data using flow decomposition. Part 2: Application to Eulerian and Lagrangian data. *J. Atmos. Oceanic Technol.*, 20, 492-512.

Chu, P.C., Ivanov, L.M., and Margolina, T.M., 2004. Rotation method for reconstructing process and field from imperfect data. *Int. J. Bifur. Chaos*, 14, 2991-2997.

Chu, P.C., and Fan, C. W., 2010. Optimal linear fitting for objective determination of ocean mixed layer depth from glider profiles. *J. Atmos. Oceanic Technol*., in press.

Hasegawa, T., and Hanawa, K., 2003. Heat content related to ENSO variability in the Pacific, *J. Phys. Oceanogr*., 33, 407– 421.

Jin, F.-F., 1997. An equatorial ocean recharge paradigm for ENSO. Part I: Conceptual model. *J. Atmos. Sci.,* **54,** 811–829.

Pielke, R. A., Jr., and Landsea, C. N., 1999. La Niña, El Niño, and hurricane damages in the United States. *Bull. Amer. Meteor. Soc.,* **80,** 2027–2033.

Rao, S. A., Behera, S. K., Masumoto, Y., and Yamagata, T. 2002. Interannual variability in the subsurface tropical Indian Ocean with a special emphasis on the Indian Ocean Dipole. Deep-Sea Res., 49B, 1549–1572.

Saji, N. H., Goswami, B. N., Vinayachandran, P. N., and Yamagata, T., 1999. A dipole in the tropical Indian Ocean. *Nature*, 401, 360–363.

Sun, C., Thresher, A., Keeley, R., Hall, N., Hamilton, M., Chinn, P., Tran, A., Goni, G., Petit de la Villeon, L., Carval, T., Cowen, L., Manzella, G., Gopalakrishna, V., Guerrero, R., Reseghetti, F., Kanno, Y., Klein, B., Rickards, L., Baldoni A., Lin, S., Ji, F., and Nagaya, Y., 2010. The data management system for the Global Temperature and Salinity Profile Program (GTSPP). In Proceedings of the "OceanObs'09: Sustained Ocean Observations and Information for Society" Conference (Vol. 2), Venice, Italy, 21-25 September 2009, Hall, J, Harrison D.E. and Stammer, D., Eds., ESA Publication WPP-306.

Vinayachandran, P. N., Saji, N. H., and Yamagata, T., 1999. Response of the equatorial Indian Ocean to an unusual wind event during 1994. *Geophys. Res. Lett.*, 26, 1613–1616.

Walker, G. T., and Bliss, E. W., 1937. World weather VI. Mem. Roy. Meteor. Soc*.,* **4,** 119–139.

Weng, H., Ashok, S. K., Behera, S., . Rao, A., Yamagata, T., 2007. Impacts of recent El Nino Modoki on dry/wet conditions in the Pacific rim during boreal summer. Clim Dyn, DOI 10.1007/s00382-007-0234-0

Yamagata, T., Behera, S. K., Rao, S. A., Guan, Z., Ashok, K., and Saji, H. N., 2002. The Indian Ocean Dipole: A physical entity. *CLIVAR Exch.,* 24, 15–18.

Yamagata, T., Ashok, K., Behera, S., Rao, S., and Weng , H., 2007. Oceans and Climate Change ―El Niño Modoki (Pseudo-El Niño) and its Impact on the World Climate Series on Sea and Human Security: "Towards a comprehensive security for seas and oceans", 14-19 October 2007, Hiroshima, Japan.